Submitted to the
HEP2005 International Europhysics Conference on High Energy Physics
EPS (July 21st-27th 2005) in Lisboa, Portugal

Abstract: 375 **Session: Hard QCD**

Inclusive-jet cross sections in deep inelastic scattering at HERA and determination of α_s

ZEUS Collaboration

Abstract

Inclusive-jet differential cross sections have been measured in neutral current deep inelastic ep scattering for boson virtualities $Q^2 > 125$ GeV^2 with the ZEUS detector at HERA using an integrated luminosity of 81.7 pb^{-1}. Jets were identified in the Breit frame using the k_T cluster algorithm in the longitudinally inclusive mode. Measurements of differential inclusive-jet cross sections are presented as functions of jet transverse energy, $E^{\rm jet}_{T,\rm B}$, jet pseudorapidity and Q^2, for jets with $E^{\rm jet}_{T,\rm B} > 8$ GeV. Next-to-leading-order (NLO) QCD calculations describe well the measurements. An NLO QCD analysis of the differential cross sections has allowed a precise determination of $\alpha_s(M_Z)$, yielding a value of $\alpha_s(M_Z) = 0.1196 \pm 0.0011$ (stat.) $^{+0.0019}_{-0.0025}$ (exp.) $^{+0.0029}_{-0.0017}$ (th.) for $Q^2 > 500$ GeV^2.

1 Introduction

Jet production in neutral current (NC) deep inelastic ep scattering (DIS) at high Q^2, where Q^2 is the negative of the square of the virtuality of the exchanged boson, provides a testing ground for perturbative QCD (pQCD). In DIS, the predictions of pQCD have the form of a convolution of matrix elements with parton distribution functions (PDFs) of the target hadron. The matrix elements describe the short-distance structure of the interaction and are calculable in pQCD at each order, whereas the PDFs contain the description of the long-distance structure of the target hadron.

The hadronic final state in NC DIS may consist of jets of high transverse energy, $E_T^{\rm jet}$, produced in the short-distance process as well as the remnant (beam jet) of the incoming proton. In this type of processes, the Breit frame [1] is preferred, since it provides a maximal separation between the products of the beam fragmentation and the hard jets. Furthermore, the contribution due to the current jet in events from the Born process is suppressed by requiring the production of jets with high $E_T^{\rm jet}$ in this frame. Jet production in the Breit frame is, therefore, directly sensitive to hard QCD processes, thus allowing direct tests of the pQCD predictions.

Jet cross sections in NC DIS have been studied previously at HERA. Inclusive-jet [2, 3], dijet [4] and multijet [5] production have been used to test pQCD and extract values of the strong coupling constant, α_s. From these determinations of $\alpha_s(M_Z)$, the smallest uncertainty was obtained in the analysis on the inclusive-jet cross sections. This arises from the fact that the inclusive-jet cross sections are infrared insensitive; for dijet or trijet cross sections restrictions on the topology of the jets are necessary to avoid the infrared-sensitive regions where the next-to-leading-order (NLO) QCD programs are not reliable. This difficulty is not present in the calculations of inclusive-jet cross sections and, thus, such measurements allow tests of pQCD in the widest phase-space region for jets. Therefore, to further reduce the uncertainties in the determination of $\alpha_s(M_Z)$, it is worth pursuing this type of measurements.

Furthermore, differential jet cross sections as a function of the jet transverse energy in the Breit frame, $E_{T,{\rm B}}^{\rm jet}$, in different regions of Q^2 [2] have been recently included in a NLO QCD fit to extract the proton PDFs [6]. They helped to reduce the uncertainty of the gluon density in the mid- to high-x region.

This paper presents new measurements of differential inclusive-jet cross sections as a function of the jet pseudorapidity in the Breit frame, $\eta_{\rm B}^{\rm jet}$, $E_{T,{\rm B}}^{\rm jet}$, Q^2 and $d\sigma/dE_{T,{\rm B}}^{\rm jet}$ in different regions of Q^2. Jets with $E_{T,{\rm B}}^{\rm jet} > 8$ GeV and $-2 < \eta_{\rm B}^{\rm jet} < 1.5$ were selected. The data sample used corresponds to 81.7 pb^{-1}, which is a more than twofold increase with respect to the previous analysis [2], yielding smaller experimental uncertainties. These new measurements probe a different kinematic regime. Lower experimental uncertainties have allowed a more accurate determination of α_s and of its running as well as a better constraint on the proton PDFs.

2 Experimental set-up

A detailed description of the ZEUS detector can be found elsewhere [7,8]. A brief outline of the components that are most relevant for this analysis is given below.

Charged particles are tracked in the central tracking detector (CTD) [9], which operates in a magnetic field of 1.43 T provided by a thin superconducting solenoid. The CTD consists of 72 cylindrical drift-chamber layers, organized in nine superlayers covering the polar-angle[1] region $15^\circ < \theta < 164^\circ$. The transverse-momentum resolution for full-length tracks can be parameterised as $\sigma(p_T)/p_T = 0.0058 p_T \oplus 0.0065 \oplus 0.0014/p_T$, with p_T in GeV. The tracking system was used to measure the interaction vertex with a typical resolution along (transverse to) the beam direction of 0.4 (0.1) cm and to cross-check the energy scale of the calorimeter.

The high-resolution uranium–scintillator calorimeter (CAL) [10] covers 99.7% of the total solid angle and consists of three parts: the forward (FCAL), the barrel (BCAL) and the rear (RCAL) calorimeters. Each part is subdivided transversely into towers and longitudinally into one electromagnetic section (EMC) and either one (in RCAL) or two (in BCAL and FCAL) hadronic sections (HAC). The smallest subdivision of the calorimeter is called a cell. Under test-beam conditions, the CAL single-particle relative energy resolutions were $\sigma(E)/E = 0.18/\sqrt{E}$ for electrons and $\sigma(E)/E = 0.35/\sqrt{E}$ for hadrons, with E in GeV.

The luminosity was measured from the rate of the bremsstrahlung process $ep \to e\gamma p$. The resulting small-angle energetic photons were measured by the luminosity monitor [11], a lead-scintillator calorimeter placed in the HERA tunnel at $Z = -107$ m.

3 Data selection and jet search

The data were collected during the running period 1998-2000, when HERA operated with protons of energy $E_p = 920$ GeV and electrons or positrons[2] of energy $E_e = 27.5$ GeV,

---

[1] The ZEUS coordinate system is a right-handed Cartesian system, with the Z axis pointing in the proton beam direction, referred to as the "forward direction", and the X axis pointing left towards the centre of HERA. The coordinate origin is at the nominal interaction point.

[2] Here and in the following, the term "electron" denotes generically both the electron (e^-) and the positron (e^+), unless otherwise stated.

and correspond to an integrated luminosity of 81.7 ± 1.9 pb^{-1}.

Neutral current DIS events were selected offline using criteria similar to those reported previously [2]. The main steps are briefly listed below.

The scattered-electron candidate was identified from the pattern of energy deposits in the CAL [12]. The energy (E'_e) and polar angle (θ_e) of the electron candidate were determined from the CAL measurements. The Q^2 variable was reconstructed from the double angle method ($Q^2_{\rm DA}$) [13], which uses θ_e and the angle γ_h, which corresponds to the angle of the scattered quark in the quark-parton model. Cuts on $\cos\gamma_h$ were applied to restrict the phase-space selection in Bjorken x and the inelasticity y, since these variables are related by

$$\cos\gamma_h = \frac{(1-y)xE_p - yE_e}{(1-y)xE_p + yE_e}.$$

The angle γ_h was reconstructed from the CAL measurements of the hadronic final state [13].

The following requirements were imposed on the data sample:

- an electron candidate of energy $E'_e > 10$ GeV;
- $y_e < 0.95$, where $y_e = 1 - E'_e(1-\cos\theta_e)/(2E_e)$;
- the total energy not associated with the electron candidate within a cone of radius 0.7 units in the pseudorapidity-azimuth ($\eta - \varphi$) plane around the electron direction should be less than 10% of the electron energy;
- for $30^\circ < \theta_e < 140^\circ$, the fraction of the electron energy within a cone of radius 0.3 units in the $\eta - \varphi$ plane around the electron direction should be larger than 0.9; for $\theta_e < 30^\circ$, the cut was raised to 0.98;
- the vertex position along the beam axis should be in the range $|Z| < 34$ cm;
- $38 < (E - p_Z) < 65$ GeV, where E is the total energy as measured by the CAL, $E = \sum_i E_i$, and p_Z is the Z-component of the vector $\boldsymbol{p} = \sum_i E_i \boldsymbol{r_i}$; in both cases the sum runs over all CAL cells, E_i is the energy of the CAL cell i and $\boldsymbol{r_i}$ is a unit vector along the line joining the reconstructed vertex and the geometric centre of the cell i;
- $p_T^{\rm miss}/\sqrt{E_T} < 2.5$ GeV$^{1/2}$, where $p_T^{\rm miss}$ is the missing transverse momentum as measured with the CAL ($p_T^{\rm miss} \equiv \sqrt{p_X^2 + p_Y^2}$) and E_T is the total transverse energy in the CAL;
- no second electron candidate with energy above 10 GeV and energy in the CAL, after subtracting that of the two electron candidates, below 4 GeV;
- $Q^2_{\rm DA} > 125$ GeV^2;
- $|\cos\gamma_h| < 0.65$.

The k_T cluster algorithm [14] was used in the longitudinally invariant inclusive mode [15] to reconstruct jets in the hadronic final state both in data and in Monte Carlo (MC) simulated events (see Section 4). In data, the algorithm was applied to the energy deposits measured in the CAL cells after excluding those associated with the scattered-electron candidate. The jet search was performed in the $\eta - \varphi$ plane of the Breit frame. The jet variables were defined according to the Snowmass convention [16].

After reconstructing the jet variables in the Breit frame, the massless four-momenta were boosted into the laboratory frame, where the transverse energy ($E^{\rm jet}_{\rm T,LAB}$) and the pseudo-rapidity ($\eta^{\rm jet}_{\rm LAB}$) of each jet were calculated. Energy corrections were then applied to the jets in the laboratory frame and propagated into $E^{\rm jet}_{T,{\rm B}}$. The jet variables in the laboratory frame were also used to apply additional cuts on the selected sample:

- events were removed from the sample if the distance of any of the jets to the electron candidate in the $\eta - \varphi$ plane of the laboratory frame, was smaller than 1 unit;
- events were removed from the sample if any of the jets was in the backward region of the detector ($\eta^{\rm jet}_{\rm LAB} < -2$);
- jets with low transverse energy in the laboratory frame ($E^{\rm jet}_{\rm T,LAB} < 2.5$ GeV) were not included in the final sample;

The final data sample contained 19640 events with at least one jet satisfying $E^{\rm jet}_{T,{\rm B}} > 8$ GeV and $-2 < \eta^{\rm jet}_{\rm B} < 1.5$.

4 Monte Carlo simulation

Samples of events were generated to determine the response of the detector to jets of hadrons and the correction factors necessary to obtain the hadron-level jet cross sections. The generated events were passed through the GEANT 3.13-based [17] ZEUS detector- and trigger-simulation programs [8]. They were reconstructed and analysed by the same program chain as the data.

Neutral current DIS events including radiative effects were simulated using the HERACLES 4.6.1 [18] program with the DJANGOH 1.1 [19] interface to the hadronisation programs. HERACLES includes corrections for initial- and final-state radiation, vertex and propagator terms, and two-boson exchange. The QCD cascade is simulated using the colour-dipole model (CDM) [20] including the leading-order (LO) QCD diagrams as implemented in ARIADNE 4.08 [21] and, as a systematic check of the final results, with the MEPS model of LEPTO 6.5 [22]. The CTEQ5D [23] proton PDFs were used for these simulations. Fragmentation into hadrons is performed using the Lund string model [24] as implemented in JETSET [25, 26]

The jet search was performed on the MC events using the energy measured in the CAL cells in the same way as for the data. Using the sample of events generated with either Ariadne or Lepto-MEPS and after applying the same offline selection as for the data, a good description of the measured distributions for the kinematic and jet variables was found. The same jet algorithm was also applied to the hadrons (partons) to obtain the predictions at the hadron (parton) level. The MC programs were used to correct the measured cross sections for QED radiative effects.

5 NLO QCD calculations

The measurements were compared with NLO QCD ($\mathcal{O}(\alpha_s^2)$) calculations obtained using the program Disent [27]. The calculations were performed in the $\overline{MS}$ renormalisation and factorisation schemes using a generalised version [27] of the subtraction method [28]. The number of flavours was set to five and the renormalisation (μ_R) and factorisation (μ_F) scales were chosen to be $\mu_R = E_{T,\rm B}^{\rm jet}$ and $\mu_F = Q$, respectively. The strong coupling constant, α_s, was calculated at two loops with $\Lambda_{\overline{MS}}^{(5)} = 220$ MeV, corresponding to $\alpha_s(M_Z) = 0.1175$. The calculations were performed using the MRST99 [29] parameterisations of the proton PDFs. The k_T cluster algorithm was also applied to the partons in the events generated by Disent in order to compute the jet cross-section predictions.

Since the measurements refer to jets of hadrons, whereas the NLO QCD calculations refer to jets of partons, the predictions were corrected to the hadron level using the MC models. The multiplicative correction factor ($C_{\rm had}$) was defined as the ratio of the cross section for jets of hadrons over that for jets of partons, estimated by using the MC programs described in Section 4. The ratios obtained with Ariadne were taken as the value of $C_{\rm had}$. The value of $C_{\rm had}$ differs from unity by less than 10%, except in the backward region of the Breit frame where it differs by up to 20%.

The NLO QCD predictions were also corrected for the Z^0-exchange contribution by using MC simulated events with and without Z^0-exchange. The multiplicative correction factor was defined as the ratio of the cross section for jets of partons obtained with both photon and Z^0 exchange over that obtained with photon exchange only.

5.1 Theoretical uncertainties

Several sources of uncertainty in the theoretical predictions were considered:

- the uncertainty on the NLO QCD calculations due to terms beyond NLO, estimated by varying μ_R between $E_{T,\rm B}^{\rm jet}/2$ and $2E_{T,\rm B}^{\rm jet}$, was $\sim \pm 5\%$;

- the uncertainty on the NLO QCD calculations due to that on $\alpha_s(M_Z)$ was estimated by repeating the calculations using two additional sets of proton PDFs, MRST99↑↑ and MRST99↓↓ [29], determined assuming $\alpha_s(M_Z) = 0.1225$ and 0.1125, respectively. The difference between the calculations using these sets and MRST99 was scaled by a factor of 0.54 to reflect the current uncertainty on the world average of α_s [30]. The resulting uncertainty in the cross sections was $\sim \pm 4\%$;
- the uncertainty in the NLO QCD calculations due to the uncertainties in the proton PDFs was estimated by repeating the calculations using 40 additional sets from CTEQ6 [31]. The resulting uncertainty in the cross sections was $\sim \pm 3\%$.

The total theoretical uncertainty was obtained by adding in quadrature the individual uncertainties listed above.

6 Systematic uncertainties

The following sources of systematic uncertainty were considered for the measured jet cross sections:

- the uncertainty in the absolute energy scale of the jets was estimated to be $\pm 1\%$ for $E^{\rm jet}_{\rm T,LAB} > 10$ GeV and $\pm 3\%$ for lower $E^{\rm jet}_{\rm T,LAB}$ values [32]. The resulting uncertainty was $\sim \pm 5\%$;
- the uncertainty in the absolute energy scale of the electron candidate was estimated to be $\pm 1\%$ [33]. The resulting uncertainty was below $\pm 1\%$;
- the differences in the results obtained by using either ARIADNE or LEPTO-MEPS to correct the data for detector effects were taken to represent systematic uncertainties. The uncertainty was below $\pm 7\%$;
- the $E^{\rm jet}_{\rm T,LAB}$ cut was raised to 4 GeV. The uncertainty was smaller than $\pm 1\%$;
- the cut in $\eta^{\rm jet}_{\rm LAB}$ used to suppress the contamination due to photons falsely identified as jets in the Breit frame was set to -3 and to -1.5. The uncertainty was below $\pm 1\%$;
- the uncertainty in the cross sections due to that in the simulation of the trigger was below 0.5%.

The systematic uncertainties not associated with the absolute energy scale of the jets were added in quadrature to the statistical uncertainties and are shown in the figures as error bars. The uncertainty due to the absolute energy scale of the jets is shown separately as a shaded band in each figure, due to the large bin-to-bin correlation.

In addition, there was an overall normalisation uncertainty of 2.3% from the luminosity determination, which is not included in the figures.

7 Results

7.1 Inclusive-jet differential cross sections

The differential inclusive-jet cross sections were measured in the kinematic region $Q^2 > 125$ GeV^2 and $|\cos\gamma_h| < 0.65$. These cross sections include every jet of hadrons in the event with $E^{\rm jet}_{T,{\rm B}} > 8$ GeV and $-2 < \eta^{\rm jet}_{\rm B} < 1.5$ and were corrected for detector and QED radiative effects.

The measurements of the differential inclusive-jet cross sections as functions of $\eta^{\rm jet}_{\rm B}$, $E^{\rm jet}_{T,{\rm B}}$ and Q^2 are presented in Figs. 1-3. The data points are plotted at the weighted mean in each bin of the corresponding variable. The measured $d\sigma/dQ^2$ ($d\sigma/dE^{\rm jet}_{T,{\rm B}}$) exhibits a steep fall-off over five (four) orders of magnitude in the Q^2 ($E^{\rm jet}_{T,{\rm B}}$) range considered.

The NLO QCD predictions are compared to the measurements in Figs. 1-3. The fractional difference of the measured differential cross sections to the NLO QCD calculations are shown in the lower part of the figures. The calculations reproduce well the measured differential cross sections.

To study the scale dependence, NLO QCD calculations using $\mu_R = Q$ are also compared to the data in Figs. 1-3; they provide a somewhat poorer description of the data than those using $\mu_R = E^{\rm jet}_{T,{\rm B}}$.

7.2 Differential $d\sigma/dE^{\rm jet}_{T,{\rm B}}$ cross section in different regions of Q^2

The measurements of the differential cross-section $d\sigma/dE^{\rm jet}_{T,{\rm B}}$ in different regions of Q^2 are presented in Fig. 4. The $E^{\rm jet}_{T,{\rm B}}$ dependence of the cross section becomes less steep as Q^2 increases. Fig. 5 shows the fractional difference of the measured differential cross sections to the NLO QCD calculations. A good description of these cross sections is also obtained.

7.3 Determination of $\alpha_s(M_Z)$

The measured differential cross-sections as functions of $E^{\rm jet}_{T,{\rm B}}$ and Q^2 were used to determine $\alpha_s(M_Z)$ using a method similar to one presented previously [2,4,5]. The NLO QCD calculations were performed using the program Disent with three different MRST99 sets of proton PDFs, central, MRST99$\downarrow\downarrow$ and MRST99$\uparrow\uparrow$; the value of $\alpha_s(M_Z)$ used in each partonic cross-section calculation was that associated with the corresponding set of PDFs. The $\alpha_s(M_Z)$ dependence of the predicted cross sections in each bin i of $E^{\rm jet}_{T,{\rm B}}$ or Q^2 was parameterised according to

$$[d\sigma/dA(\alpha_s(M_Z))]_i = C_1^i \alpha_s(M_Z) + C_2^i \alpha_s^2(M_Z),$$

where C_1^i and C_2^i were determined from a χ^2 fit by using the NLO QCD calculations corrected for hadronisation and Z^0-exchange effects and $A = E_{T,\mathrm{B}}^{\mathrm{jet}}$ or Q^2. Finally, a value of $\alpha_s(M_Z)$ was determined in each $E_{T,\mathrm{B}}^{\mathrm{jet}}$ or Q^2 region as well as from all the data points by a χ^2 fit.

The uncertainties on the extracted values of $\alpha_s(M_Z)$ due to the experimental systematic uncertainties were evaluated by repeating the analysis for each systematic check presented in Section 6. The largest contribution to the experimental uncertainty comes from the jet energy scale and amounts to $\pm 1.5\%$ on $\alpha_s(M_Z)$. The theoretical uncertainties were evaluated as described in Section 5.1. The largest contribution was the theoretical uncertainty on $\alpha_s(M_Z)$ arising from terms beyond NLO, which was $^{+1.1}_{-1.6}\%$. The uncertainty on $\alpha_s(M_Z)$ due to the uncertainties on the proton PDFs was $\pm 1\%$. The total theoretical uncertainty on $\alpha_s(M_Z)$ was obtained by adding these uncertainties in quadrature.

The values of $\alpha_s(M_Z)$ as determined from the measured $d\sigma/dE_{T,\mathrm{B}}^{\mathrm{jet}}$ in each region of E_T^{jet} and from the measured $d\sigma/dQ^2$ in each region of Q^2 are shown in Figs. 6(a) and (c), respectively. By combining all the $E_{T,\mathrm{B}}^{\mathrm{jet}}$ regions, the value of $\alpha_s(M_Z)$ obtained is

$$\alpha_s(M_Z) = 0.1201 \pm 0.0006 \text{ (stat.) } ^{+0.0033}_{-0.0038} \text{ (exp.) } ^{+0.0049}_{-0.0032} \text{ (th.)},$$

and combining all the Q^2 regions,

$$\alpha_s(M_Z) = 0.1198 \pm 0.0006 \text{ (stat.) } ^{+0.0034}_{-0.0039} \text{ (exp.) } ^{+0.0049}_{-0.0033} \text{ (th.)}.$$

The best determination of $\alpha_s(M_Z)$ was obtained by using the measured $d\sigma/dQ^2$ for $Q^2 > 500$ GeV^2, as in the previous publication [2], for which both the theoretical and total uncertainties in $\alpha_s(M_Z)$ are minimised. The value obtained is

$$\alpha_s(M_Z) = 0.1196 \pm 0.0011 \text{ (stat.) } ^{+0.0019}_{-0.0025} \text{ (exp.) } ^{+0.0029}_{-0.0017} \text{ (th.)}.$$

These values of $\alpha_s(M_Z)$ are consistent with each other and with the current world average [30] of 0.1182 ± 0.0027 as well as with previous determinations from jet production in NC DIS at HERA [2–5]. They have a precision comparable to the values obtained from e^+e^- interactions [34].

7.4 Energy-scale dependence of α_s

The QCD prediction for the energy-scale dependence of the strong coupling constant was tested by determining α_s from the measured $d\sigma/dE_{T,\mathrm{B}}^{\mathrm{jet}}$ at different $E_{T,\mathrm{B}}^{\mathrm{jet}}$ values and from the measured $d\sigma/dQ^2$ at different Q^2 values. The method employed was the same as described above, but parameterising the α_s dependence of $d\sigma/dE_{T,\mathrm{B}}^{\mathrm{jet}}$ and $d\sigma/dQ^2$ in terms of $\alpha_s(\langle E_{T,\mathrm{B}}^{\mathrm{jet}}\rangle)$ and $\alpha_s(\langle Q\rangle)$, respectively, instead of $\alpha_s(M_Z)$, where $\langle E_{T,\mathrm{B}}^{\mathrm{jet}}\rangle$ ($\langle Q\rangle$)is the weighted mean of $E_{T,\mathrm{B}}^{\mathrm{jet}}$ (Q) in each bin. For the energy-scale dependence as a function of Q, the NLO calculations used had $\mu_R = Q$. The measured $\alpha_s(E_{T,\mathrm{B}}^{\mathrm{jet}})$ and $\alpha_s(Q)$ values are shown in Fig. 7. The results are in good agreement with the predicted running of the strong coupling constant over a large range in $E_{T,\mathrm{B}}^{\mathrm{jet}}$ and Q.

8 Summary

Measurements of the differential cross sections for inclusive-jet production in neutral current deep inelastic ep scattering at a centre-of-mass energy of 318 GeV have been presented. The cross sections refer to jets of hadrons identified in the Breit frame with the k_T cluster algorithm in the longitudinally invariant inclusive mode. The cross sections are given in the kinematic region of $Q^2 > 125$ GeV^2 and $|\cos\gamma_h| < 0.65$.

The NLO QCD calculations provide a good description of the measured differential cross sections for inclusive-jet production.

A QCD fit of the measured cross section as a function of Q^2 for $Q^2 > 500$ GeV^2 yields

$$\alpha_s(M_Z) = 0.1196 \pm 0.0011 \text{ (stat.) } {}^{+0.0019}_{-0.0025} \text{ (exp.) } {}^{+0.0029}_{-0.0017} \text{ (th.).}$$

This value is in good agreement with the world average and is at least as precise as any other individual measurement.

The QCD prediction for the energy-scale dependence of the strong coupling constant has been tested. The results are in good agreement with the predicted running of the strong coupling constant over a large range in $E_{T,\mathrm{B}}^{\mathrm{jet}}$ and Q.

Acknowledgements

We thank the DESY Directorate for their strong support and encouragement. The remarkable achievements of the HERA machine group were essential for the successful completion of this work and are greatly appreciated.

References

[1] R.P. Feynman, *Photon-Hadron Interactions*. Benjamin, New York, (1972); K.H. Streng, T.F. Walsh and P.M. Zerwas, Z. Phys. **C 2**, 237 (1979).

[2] ZEUS Coll., S. Chekanov et al., Phys. Lett. **B 547**, 164 (2002).

[3] H1 Coll., C. Adloff et al., Eur. Phys. J. **C 19**, 289 (2001).

[4] ZEUS Coll., J. Breitweg et al., Phys. Lett. **B 507**, 70 (2001).

[5] ZEUS Coll., S. Chekanov et al., Preprint DESY-05-019 (hep-ex/0502007), DESY, 2005.

[6] ZEUS Coll., S. Chekanov et al., Preprint DESY-05-050 (hep-ph/0503274), DESY, 2005.

[7] ZEUS Coll., M. Derrick et al., Phys. Lett. **B 293**, 465 (1992).

[8] ZEUS Coll., U. Holm (ed.), *The ZEUS Detector*. Status Report (unpublished), DESY (1993), available on `http://www-zeus.desy.de/bluebook/bluebook.html`.

[9] N. Harnew et al., Nucl. Inst. Meth. **A 279**, 290 (1989); B. Foster et al., Nucl. Phys. Proc. Suppl. **B 32**, 181 (1993); B. Foster et al., Nucl. Inst. Meth. **A 338**, 254 (1994).

[10] M. Derrick et al., Nucl. Inst. Meth. **A 309**, 77 (1991); A. Andresen et al., Nucl. Inst. Meth. **A 309**, 101 (1991); A. Caldwell et al., Nucl. Inst. Meth. **A 321**, 356 (1992); A. Bernstein et al., Nucl. Inst. Meth. **A 336**, 23 (1993).

[11] J. Andruszków et al., Preprint DESY-92-066, DESY, 1992; ZEUS Coll., M. Derrick et al., Z. Phys. **C 63**, 391 (1994); J. Andruszków et al., Acta Phys. Pol. **B 32**, 2025 (2001).

[12] H. Abramowicz, A. Caldwell and R. Sinkus, Nucl. Inst. Meth. **A 365**, 508 (1995); R. Sinkus and T. Voss, Nucl. Inst. Meth. **A 391**, 360 (1997).

[13] S. Bentvelsen, J. Engelen and P. Kooijman, *Proc. of the Workshop on Physics at HERA*, W. Buchmüller and G. Ingelman (eds.), Vol. 1, p. 23. Hamburg, Germany, DESY (1992); K.C. Höger, ibid., p. 43.

[14] S. Catani et al., Nucl. Phys. **B 406**, 187 (1993).

[15] S.D. Ellis and D.E. Soper, Phys. Rev. **D 48**, 3160 (1993).

[16] J.E. Huth et al., *Research Directions for the Decade. Proc. of Summer Study on High Energy Physics, 1990*, E.L. Berger (ed.), p. 134. World Scientific (1992). Also in preprint FERMILAB-CONF-90-249-E.

[17] R. Brun et al., GEANT3, Technical Report CERN-DD/EE/84-1, CERN, 1987.

[18] A. Kwiatkowski, H. Spiesberger and H.-J. Möhring, Comp. Phys. Comm. **69**, 155 (1992);
H. Spiesberger, *An Event Generator for ep Interactions at HERA Including Radiative Processes (Version 4.6)*, 1996, available on
`http://www.desy.de/~hspiesb/heracles.html`.

[19] K. Charcuła, G.A. Schuler and H. Spiesberger, Comp. Phys. Comm. **81**, 381 (1994);
H. Spiesberger, HERACLES *and* DJANGOH*: Event Generation for ep Interactions at HERA Including Radiative Processes*, 1998, available on
`http://www.desy.de/~hspiesb/djangoh.html`.

[20] Y. Azimov et al., Phys. Lett. **B 165**, 147 (1985);
G. Gustafson, Phys. Lett. **B 175**, 453 (1986);
G. Gustafson and U. Pettersson, Nucl. Phys. **B 306**, 746 (1988);
B. Andersson et al., Z. Phys. **C 43**, 625 (1989).

[21] L. Lönnblad, Comp. Phys. Comm. **71**, 15 (1992);
L. Lönnblad, Z. Phys. **C 65**, 285 (1995).

[22] G. Ingelman, A. Edin and J. Rathsman, Comp. Phys. Comm. **101**, 108 (1997).

[23] H.L. Lai et al., Eur. Phys. J. **C 12**, 375 (2000).

[24] B. Andersson et al., Phys. Rep. **97**, 31 (1983).

[25] T. Sjöstrand, Comp. Phys. Comm. **82**, 74 (1994);
T. Sjöstrand et al., Comp. Phys. Comm. **135**, 238 (2001).

[26] T. Sjöstrand, Comp. Phys. Comm. **39**, 347 (1986);
T. Sjöstrand and M. Bengtsson, Comp. Phys. Comm. **43**, 367 (1987).

[27] S. Catani and M.H. Seymour, Nucl. Phys. **B 485**, 291 (1997). Erratum in Nucl. Phys. **B 510**, 503 (1998).

[28] R.K. Ellis, D.A. Ross and A.E. Terrano, Nucl. Phys. **B 178**, 421 (1981).

[29] A.D. Martin et al., Eur. Phys. J. **C 4**, 463 (1998);
A.D. Martin et al., Eur. Phys. J. **C 14**, 133 (2000).

[30] S. Bethke, Preprint hep-ex/0407021, 2004.

[31] J. Pumplin et al., JHEP **0207**, 012 (2002);
D. Stump et al., JHEP **0310**, 046 (2003).

[32] ZEUS Coll., S. Chekanov et al., Phys. Lett. **B 531**, 9 (2002);
ZEUS Coll., S. Chekanov et al., Eur. Phys. J. **C 23**, 615 (2002);
M. Wing (on behalf of the ZEUS Coll.), *Proc. of the 10th International Conference*

on Calorimetry in High Energy Physics, R. Zhu (ed.), p. 767. Pasadena, USA (2002). Also in preprint hep-ex/0206036.

[33] ZEUS Coll., S. Chekanov et al., Eur. Phys. J. **C 21**, 443 (2001).

[34] S. Bethke, J. Phys. **G 26**, R27 (2000). Updated in Preprint hep-ex/0211012, 2002.

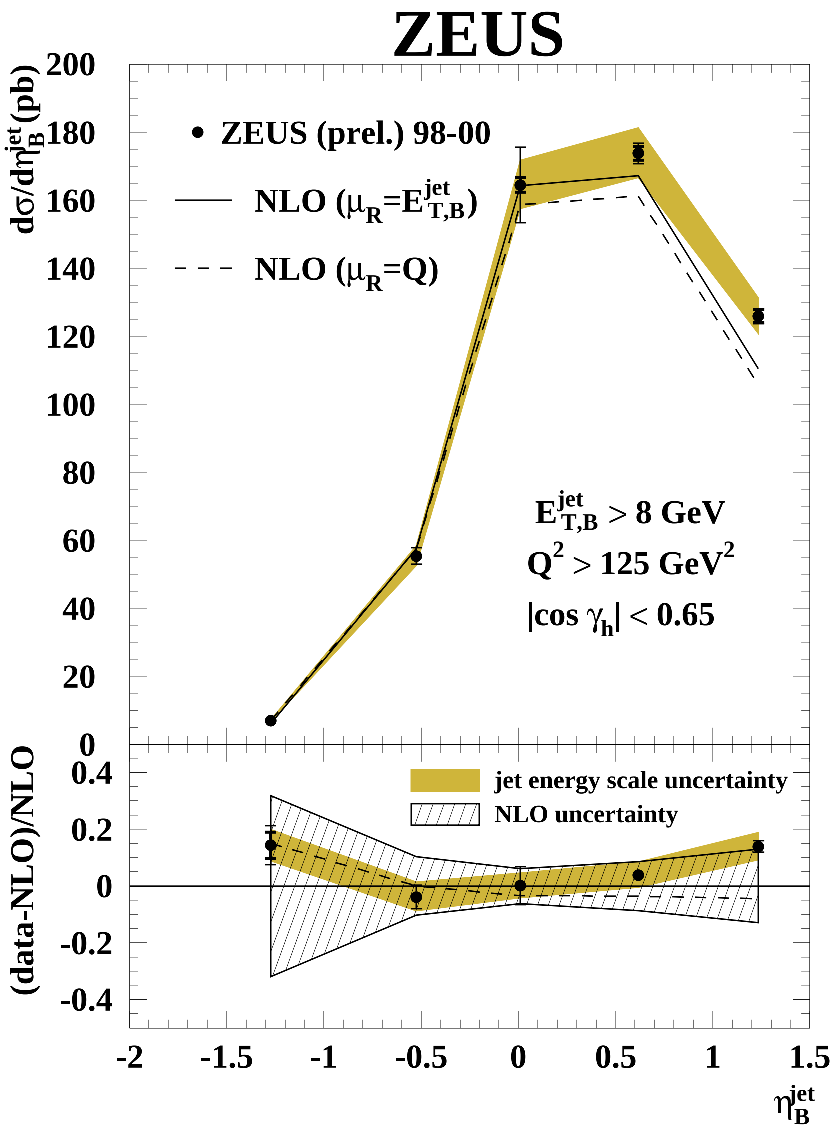

Figure 1: *The measured differential cross-section $d\sigma/d\eta_{\rm B}^{\rm jet}$ for inclusive-jet production with $E_{T,{\rm B}}^{\rm jet} > 8$ GeV (dots), in the kinematic range given by $Q^2 > 125$ GeV^2 and $|\cos\gamma_h| < 0.65$. The inner error bars represent the statistical uncertainty. The outer error bars show the statistical and systematic uncertainties, not associated with the uncertainty in the absolute energy scale of the jets, added in quadrature. The shaded band displays the uncertainty due to the absolute energy scale of the jets. The NLO QCD calculations with $\mu_R = E_{T,{\rm B}}^{\rm jet}$ (solid line) and $\mu_R = Q$ (dashed line), corrected for hadronisation and Z^0 effects and using the MRST99 parameterisations of the proton PDFs, are also shown. The lower part of the figure shows the fractional difference between the measured $d\sigma/d\eta_{\rm B}^{\rm jet}$ and the NLO QCD calculation with $\mu_R = E_{T,{\rm B}}^{\rm jet}$; the hatched band displays the total theoretical uncertainty.*

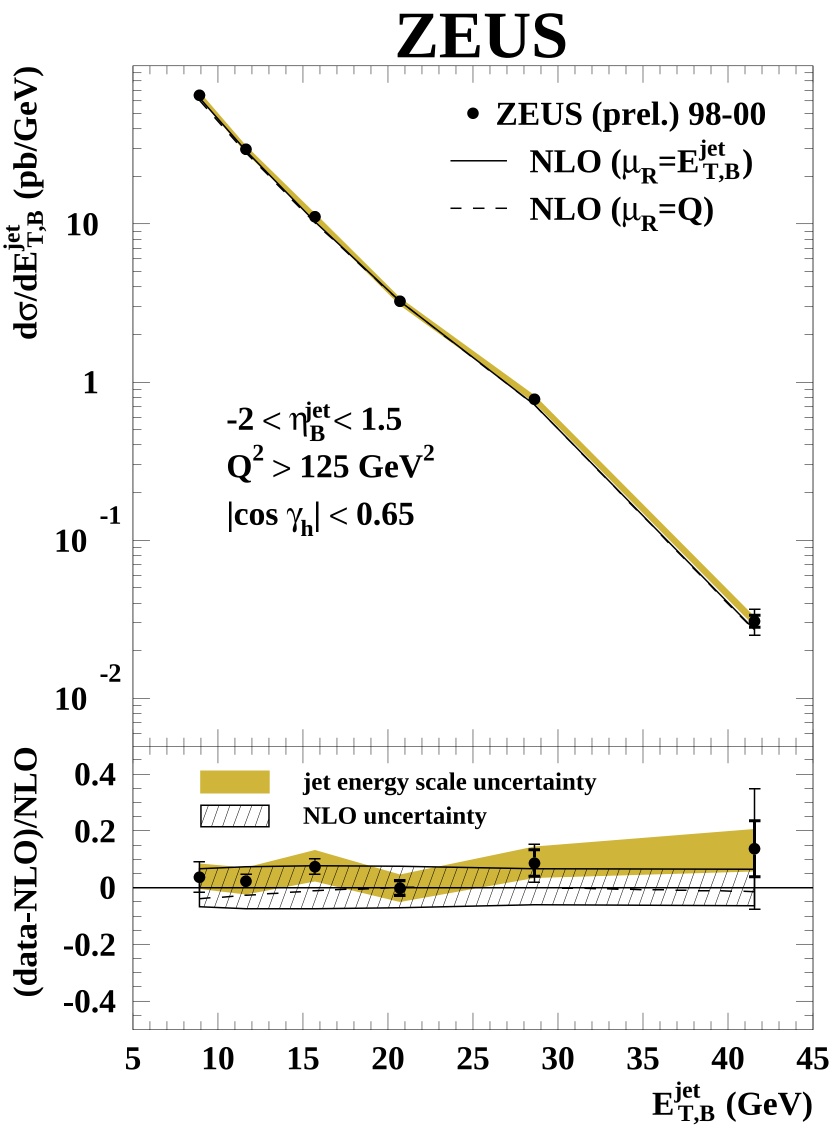

Figure 2: *The measured differential cross-section $d\sigma/dE_{T,\mathrm{B}}^{\mathrm{jet}}$ for inclusive-jet production with $-2 < \eta_{\mathrm{B}}^{\mathrm{jet}} < 1.5$ (dots), in the kinematic range given by $Q^2 > 125$ GeV^2 and $|\cos\gamma_h| < 0.65$. Other details as in the caption to Fig. 1.*

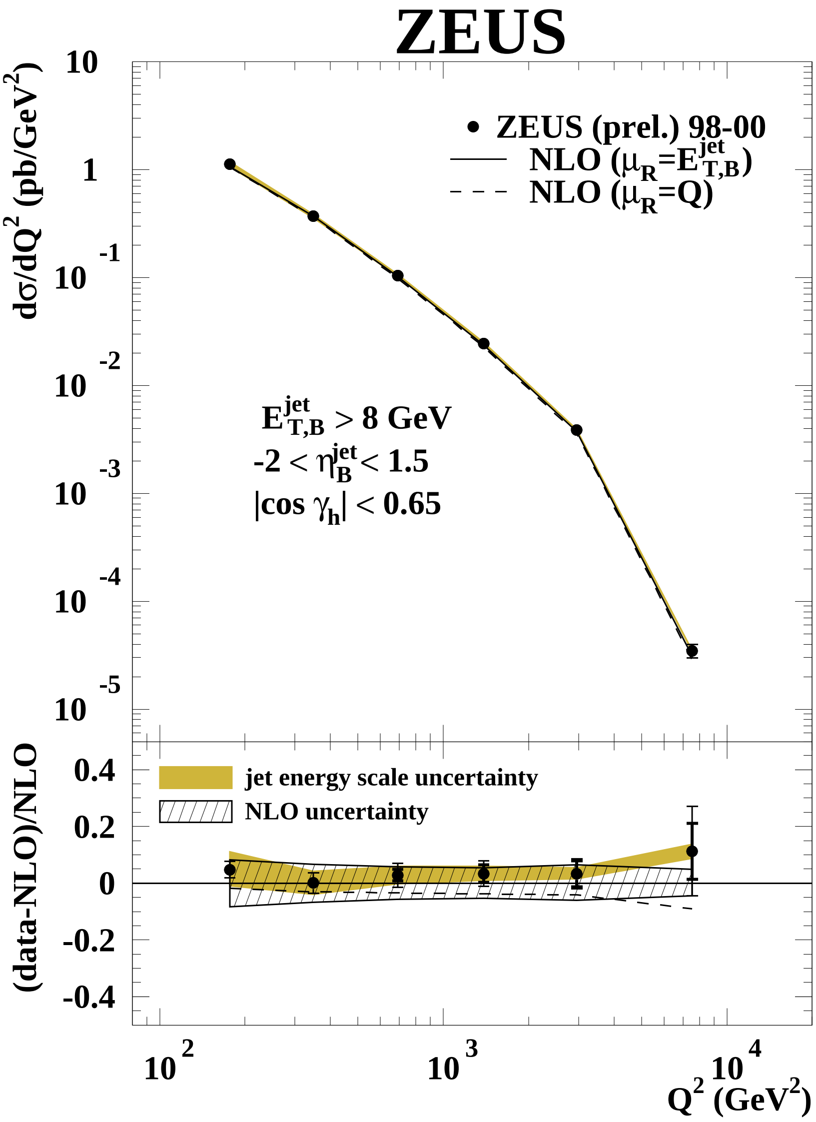

Figure 3: *The measured differential cross-section $d\sigma/dQ^2$ for inclusive-jet production with $E^{\rm jet}_{T,\rm B} > 8$ GeV and $-2 < \eta^{\rm jet}_{\rm B} < 1.5$ (dots), in the kinematic range given by $|\cos\gamma_h| < 0.65$. Other details as in the caption to Fig. 1.*

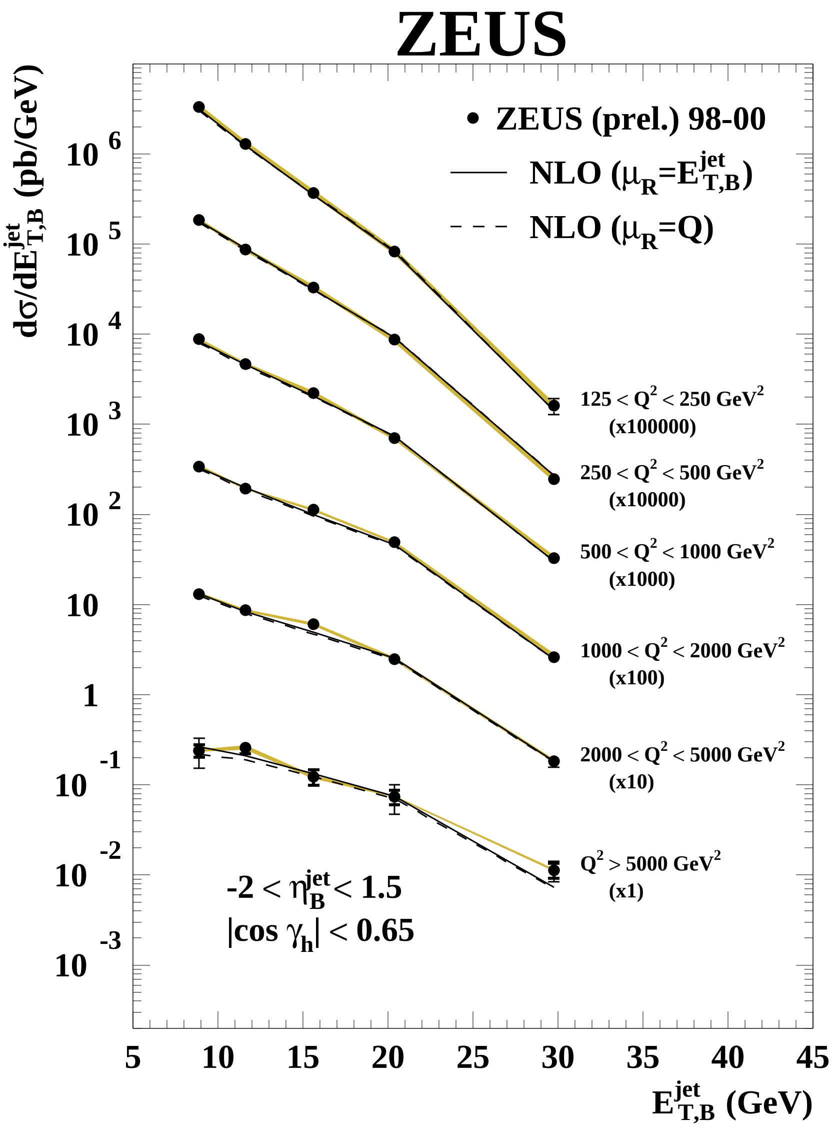

Figure 4: *The measured differential cross-section $d\sigma/dE^{\rm jet}_{T,\rm B}$ for inclusive-jet production with $-2 < \eta^{\rm jet}_{\rm B} < 1.5$ in different regions of Q^2 (dots), in the kinematic range given by $|\cos\gamma_h| < 0.65$. Each cross section has been multiplied by the scale factor indicated in brackets to aid visibility. Other details as in the caption to Fig. 1.*

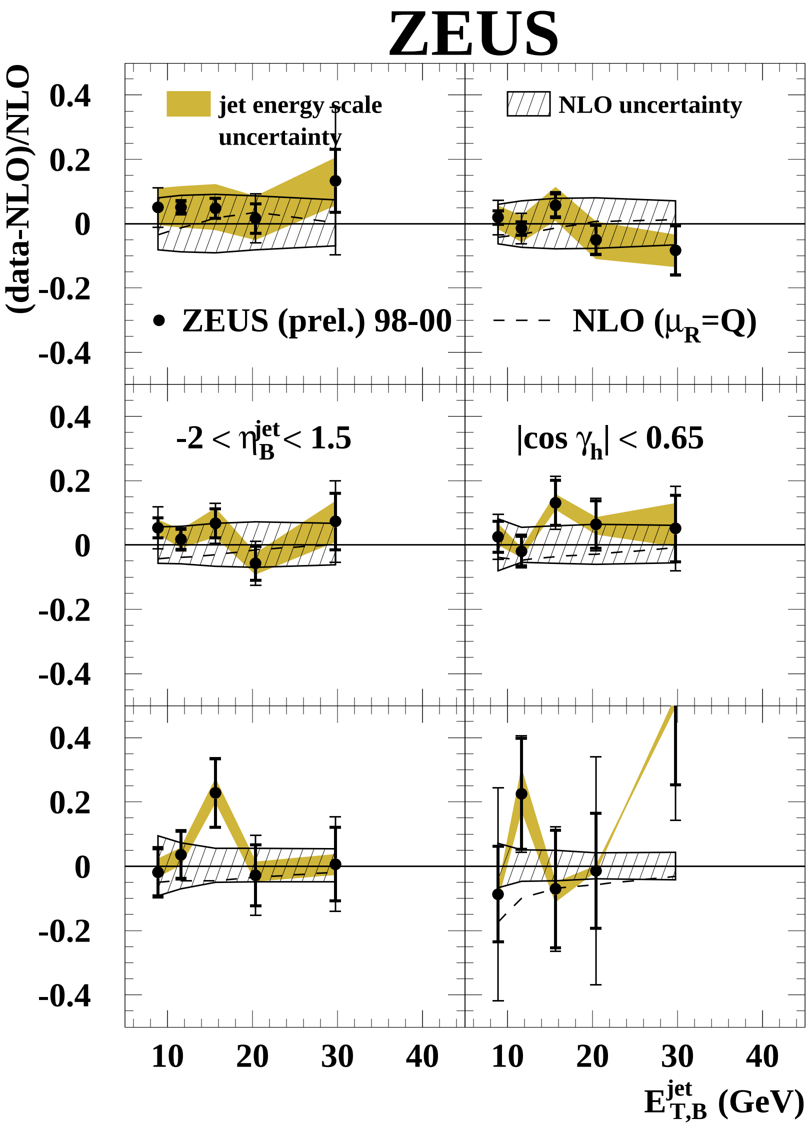

Figure 5: *Fractional difference between the measured differential cross-sections $d\sigma/dE_{T,\mathrm{B}}^{\mathrm{jet}}$ presented in Fig. 4 and the NLO QCD calculations with $\mu_R = E_{T,\mathrm{B}}^{\mathrm{jet}}$ (dots). Other details as in the caption to Fig. 1.*

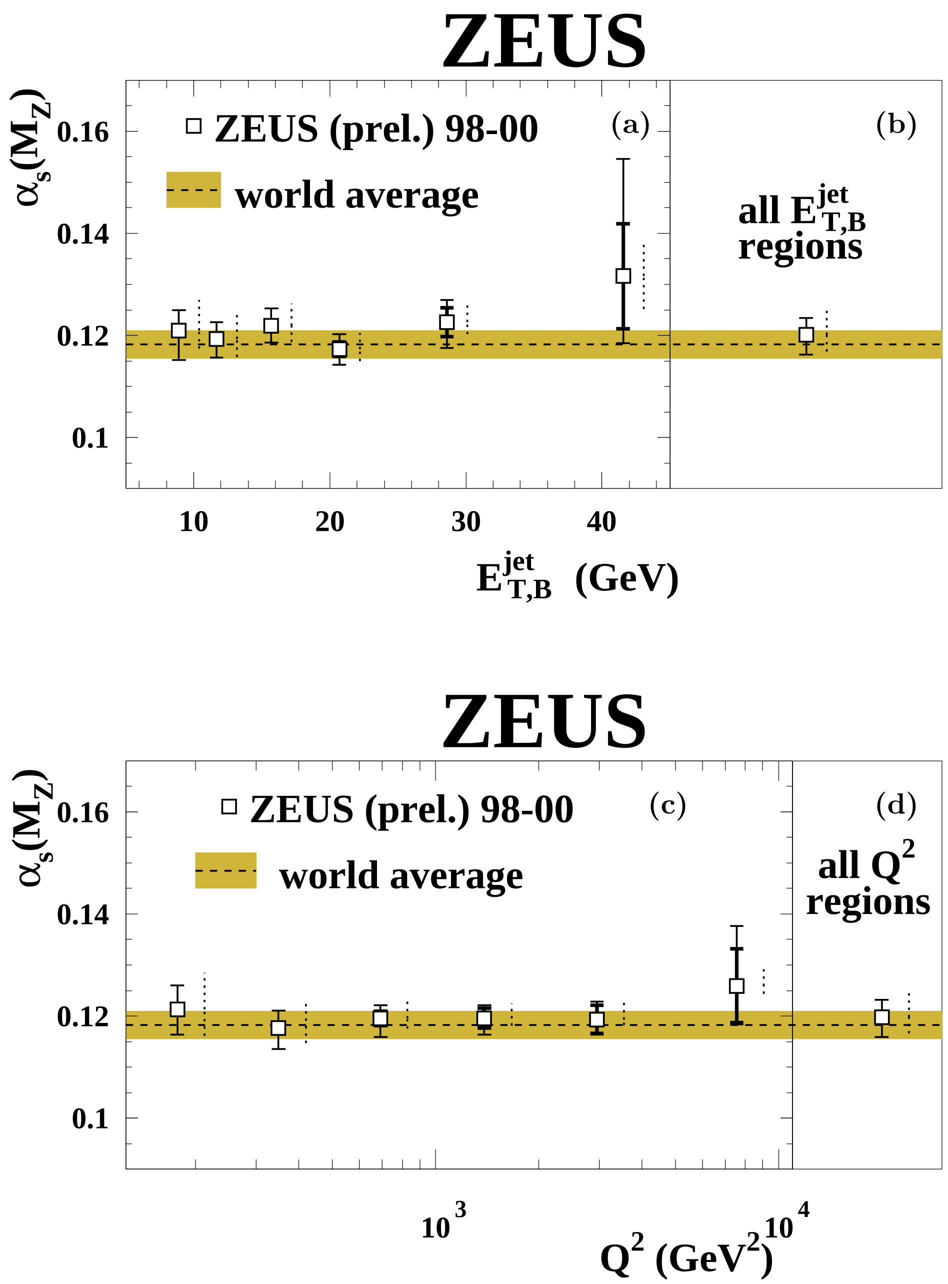

Figure 6: *The $\alpha_s(M_Z)$ values determined from the QCD fit of the measured (a) $d\sigma/dE_{T,\mathrm{B}}^{\mathrm{jet}}$ in the different $E_{T,\mathrm{B}}^{\mathrm{jet}}$ regions and (c) $d\sigma/dQ^2$ in the different Q^2 regions (squares). The combined value of $\alpha_s(M_Z)$ obtained using all the (b) $E_{T,\mathrm{B}}^{\mathrm{jet}}$ and (d) Q^2 regions (square). In all plots, the inner error bars represent the statistical uncertainties of the data. The outer error bars show the statistical and systematic uncertainties added in quadrature. The dotted vertical bars represent the theoretical uncertainties. The shaded bands display the $\alpha_s(M_Z)$ current world average [30] and its associated uncertainty.*

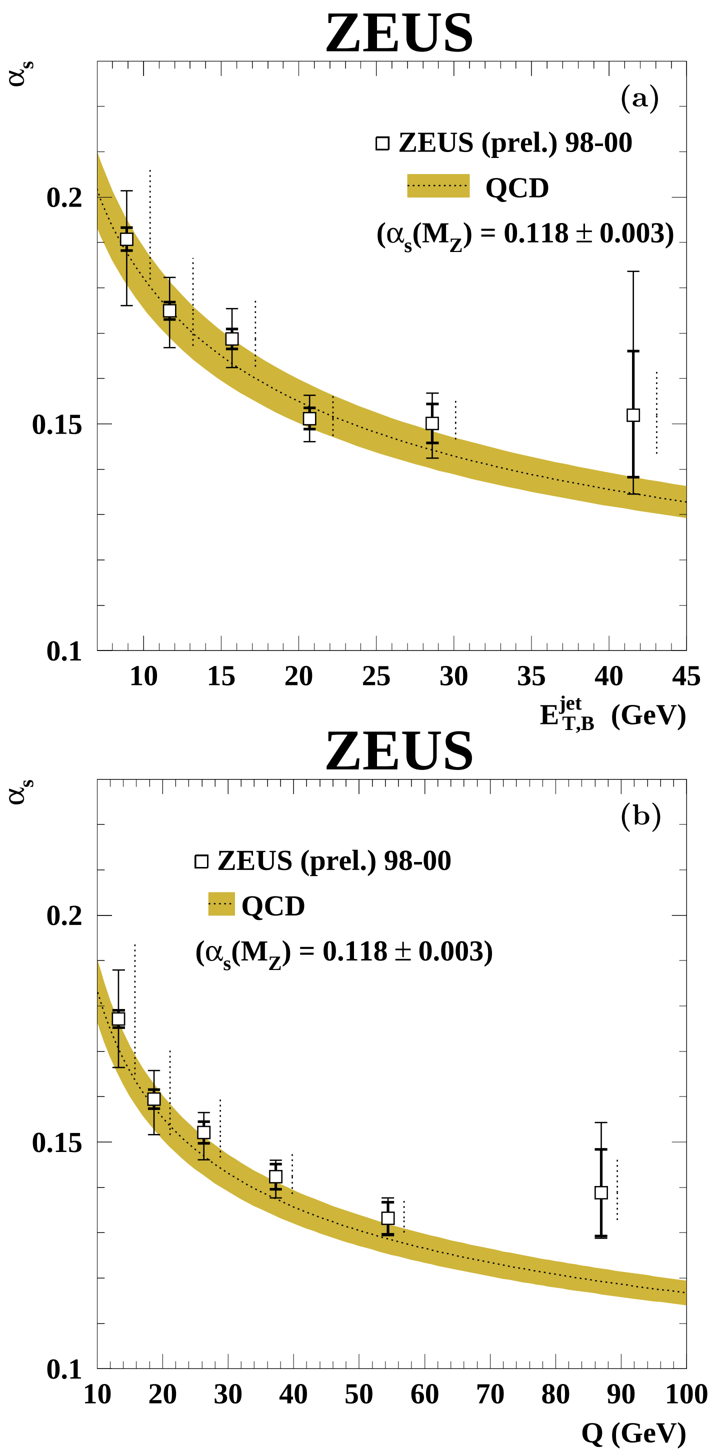

Figure 7: *(a) The $\alpha_s(E_{T,\mathrm{B}}^{\mathrm{jet}})$ values determined from the QCD fit of the measured $d\sigma/dE_{T,\mathrm{B}}^{\mathrm{jet}}$ as a function of $E_{T,\mathrm{B}}^{\mathrm{jet}}$. (b) The $\alpha_s(Q)$ values determined from the QCD fit of the measured $d\sigma/dQ^2$ as a function of Q. In both figures, the inner error bars represent the statistical uncertainty of the data. The outer error bars show the statistical and systematic uncertainties added in quadrature. The dotted error bars display the theoretical uncertainties. The shaded area indicates the renormalisation group predictions obtained from the $\alpha_s(M_Z)$ current world average [30] and its associated uncertainty.*